

Received 25 June 2023, accepted 17 July 2023, date of publication 20 July 2023, date of current version 2 August 2023.

Digital Object Identifier 10.1109/ACCESS.2023.3297271

RESEARCH ARTICLE

3-D Printed THz Waveguide Components

LIYAN ZHU¹, SANG-HEE SHIN², (Member, IEEE), ROSHAN PAYAPULLI¹,
IAN W. ROSSUCK¹, NORBERT KLEIN³, NICK M. RIDLER², (Fellow, IEEE),
AND STEPAN LUCYSZYN¹, (Fellow, IEEE)

¹Department of Electrical and Electronic Engineering, Imperial College London, SW7 2AZ London, U.K.

²Department of Electromagnetic and Electrochemical Technologies, National Physical Laboratory, TW11 0LW Teddington, U.K.

³Department of Materials, Imperial College London, SW7 2AZ London, U.K.

Corresponding author: Stepan Lucyszyn (s.lucyszyn@imperial.ac.uk)

This work was supported by the U.K. Space Agency's Centre for Earth Observation Instrumentation (CEOI) under Grant RP10G0435A202.

ABSTRACT This paper presents the state-of-the-art in polymer-based 3-D printing of metal-pipe rectangular waveguides (MPRWGs) with the first reported terahertz filters, all operating within the WR-2.2 band (325 to 500 GHz): a 5 mm-long thru line, two 399 GHz single-cavity resonators and two 403 GHz bandpass filters (BPFs). Our thru line exhibits a measured average insertion loss of only 0.9 dB, with a worst-case return loss of 13.3 dB, across the band. The single-cavity resonators, without and with corner rounding compensation (CRC) are investigated with the use of an *RLC* equivalent circuit model. The uncompensated resonator exhibits a 2.3% frequency downshift and an increase of 10.8 GHz in its 3 dB bandwidth. The compensated resonator exhibits a 2.2% frequency upshift and an increase of only 2.2 GHz in its 3 dB bandwidth; clearly demonstrating that CRC helps to mitigate against increased coupling into the resonators, as a result of manufacturing limitations with low-cost 3-D printing. Finally, the 3rd order Butterworth and Chebyshev MPRWG BPFs both have a measured passband insertion loss of only 1.0 dB. The Butterworth filter exhibits a 0.8% passband frequency upshift and worst-case return loss of 16.6 dB; while the Chebyshev filter exhibits a 1.2% passband frequency downshift and worst-case return loss of 10.4 dB. With our low-cost polymer-based 3-D printing technology, we have demonstrated measured performances that are better than those using metal-based 3-D printing in the WR-2.2 band and this may, in the not too distant future, challenge components manufactured using traditional machining technologies.

INDEX TERMS Additive manufacturing, 3-D printing, millimeter-wave, terahertz, WR-2.2, WM-570, rectangular waveguide, waveguide filter.

I. INTRODUCTION

3-D printing represents one form of additive manufacturing. Over the past four decades, interest in 3-D printing has increased exponentially within academia and industry; mainly because of its design flexibility, lightweight structures, rapid prototyping and low manufacturing cost. This emerging technology can be classified into two main categories: (i) polymer-based 3-D printing (e.g., fused deposition modeling (FDM), polymer jetting (PolyJet), stereolithography apparatus (SLA) and masked stereolithography apparatus (MSLA)); and (ii) metal-based 3-D printing (e.g., selective laser melting (SLM), micro laser sintering (MLS), as well

as other derivatives). Both polymer- and metal-based 3-D printing have demonstrated applications at microwave and millimeter-wave frequencies, making them suitable candidates for future 5G+ mobile communications, radar and imaging systems.

When comparing these two categories, metal-based 3-D printing provides good structural strength. This makes it more suitable for applications requiring high mechanical tolerances. However, even when printing with copper powder, its surface roughness is the main limitation for realizing low-loss waveguide components at sub-terahertz/upper-millimeter-wave (*ca.* 100 to 300 GHz) [1], [2] and terahertz/submillimeter-wave (300 GHz to 3 THz) [3], [4] frequencies. In contrast, polymer-based 3-D printing exhibits limited physical strength and inherently requires

The associate editor coordinating the review of this manuscript and approving it for publication was Chaker Larabi¹.

TABLE 1. Terahertz 3-D printed waveguide thru lines. (*Nominal worst-case insertion loss found at the lower band-edge frequency for COTS lines).

Frequency Range [Waveguide Band]	α'_p (dB/m)	RL (dB)	Length (mm)	Split-Block	3-D Printing Technology	Metal Plating Technology	Year	Ref.
220-325 [WR-3]	13	-	25	No	SLA	Custom-developed Cu plated	2014	[17]
	31*	-	100		COTS	Au	2023	[16]
	36†	-	25.4		RECILS	3.6 μm Ni, Cu and Au electroless	2022	[18]
	91	12	7.8		M-MAM	Cu electroplating	2021	[19]
	120	-	50		SLM (Cu-15Sn)	None	2016	[20]
	300	-	10		SLM (SS-316L)	None	2018	[21]
325-500 [WR-2.2]	61*	-	100	COTS	Au		[16]	
	157	13	5	H-plane a -edge	MSLA	5 μm Cu electroplating	2023	This New Work
	199	-	6	No	M-MAM	Cu electroplating	2021	[19]
500-750 [WR-1.5]	440	-	25	H-plane a -edge	PolyJet	500 nm Cu sputter coating	2017	Our Old Work
	115*	-	100	COTS	Au		2023	[16]
	240	7	5	No	RECILS	1 μm Ag electroplating	2017	Our Old Work
750-1100 [WR-1]	230*	-	100	COTS	Au		2023	[16]
	1,400	6	5	No	RECILS	1 μm Ag electroplating	2017	Our Old Work

† Measured using an uncalibrated photonics-based terahertz source (employing two bespoke single-mode lasers and MPRWG-packaged uni-traveling-carrier photodiode) and power meter, with maximum in-band variation of ± 10 dB/m.

additional electro(less)-plating to establish conducting walls. Nevertheless, this technology has greater potential for applications where smooth surface, low mass and low manufacturing cost are the main drivers. To this end, the authors have previously demonstrated examples of metal-pipe rectangular waveguide (MPRWG) components and subsystems, using a variety of polymer-based 3-D printing technologies, in different bands: X-band (8 to 12 GHz) using FDM [5]; Ku-band (12 to 18 GHz) using expensive PolyJet [6]; W-band (75 to 110 GHz) using SLA [5] and MSLA [7]; D-band (110 to 170 GHz) using MSLA [8]; G-band (140 to 220 GHz) using PolyJet [9] and MSLA [10], [11]; WR-2.2 band (325 to 500 GHz), also referred to as the WM-570 band by the IEEE, using PolyJet [12]; WR-1.5 band (500 to 750 GHz) and WR-1 band (750 GHz to 1.1 THz) using experimental RECILS [13]. In addition, all within the last three years, a G-band multi-channel front-end subsystem [14] has been successfully demonstrated by combining MPRWG [11] and quasi-optical components [15]; using a mixture of polymer-based 3-D printing technologies.

Our previous research has shown that iris corner rounding associated with an inductively-coupled waveguide bandpass filter (BPF), can degrade performance (e.g., center frequency shifting and bandwidth increasing) significantly with the use of a low-cost 3-D printer [11]. This becomes more significant when dealing with waveguide components as frequencies increase. To mitigate against this effect, iris corner rounding compensation (CRC) [11] is employed in this work.

For the first time, this paper demonstrates the design, manufacture and test of terahertz MPRWG filters, fabricated using an ultra-low-cost polymer-based MSLA 3-D printer having a pixel resolution of 22 μm in the x - y build plane. Three types of waveguide components (i.e., thru line, single-cavity resonators and bandpass filters), all having a flange-to-flange length of 5 mm and operating within the WR-2.2 band are investigated.

II. LITERATURE REVIEW

A. THRU LINES

The thru line is our most basic waveguide component. Terahertz (THz) commercial-off-the-shelf (COTS) MPRWG thru lines are normally manufactured using precision-machined processes. The submillimeter-wave seamless (single-block) waveguide product range from Flann Microwave Ltd. includes low loss COTS thru lines operating up to 1.1 THz [16]. The nominal insertion loss, measured at the lower band edge frequency, is shown in Table 1. Either copper or nickel is electroformed (formative) to create the MPRWG, having a quoted internal mean profile surface roughness of $R_a < 0.2 \mu\text{m}$ [16]. Information on the loss modeling of these commercial thru lines has been previously reported [11].

An exhaustive literature survey of THz 3-D printed MPRWG thru lines has been recently undertaken [11]. To the best of our knowledge, Table 1 summarizes all the MPRWG thru lines that have been reported in the open literature. Table 1 is an updated version of our earlier survey [11].

TABLE 2. Terahertz 3-D printed waveguide bandpass filters.

f_c (GHz)	Frequency Shift (GHz)	3 dB FBW (%)	Filter Order	IL (dB)	RL (dB)	$Q_L = \frac{1}{3 \text{ dB } FBW}$	Split Block	3-D Printing Technology	Metal Plating Technology	Year	Ref.
297	-3	12.8	5 th	1.1	10	7.8	E-plane	SLM (SS-316L)	3 μm Au electroless	2021	[3]
314	+14	9.5		3.0	11	10.5	4-layer assembly	Screen Printing (W-Cu)	None	2022	[4]
399	-5	16.4	3 rd	1.0	10	6.1	H-plane <i>a</i> -edge	MSLA	5 μm Cu electroplating	2023	This New Work
406	+3	15.8			16	6.3					

Only seven examples of 3-D printed thru lines operate at WR-3 (220 to 325 GHz) and higher frequency bands; all previously reported within the last decade (since 2014). Here, α'_D and RL refer to the average dissipative attenuation per unit length and the worst-case return loss (RL) across the associated waveguide band, respectively. For the WR-3 band, there are two examples using polymer-based printing (i.e., SLA [17] and RECILS [18]) and three examples using expensive metal-based solutions (i.e., micro metal additive manufacturing (M-MAM) [19] and SLM [20], [21]). Note that, even though M-MAM does not involve 3-D printing (being formative), [19] is included in Table 1 for comparison against the more relevant additive manufacturing technologies.

In the WR-3 band, it can be seen that polymer-based thru lines show relatively good performance, with band-average dissipative attenuation being 13 dB/m [17] and 36 dB/m [18]; the COTS thru line has a worst-case value of 31 dB/m [16]. In contrast, metal-based 3-D printed thru lines exhibit a higher band-average $\alpha'_D > 90$ dB/m [19], [20], [21]. This is mainly due to the low effective bulk DC conductivity (dictated by the intrinsic conductivity of the metal powder and extrinsic surface roughness).

For the WR-2.2 band of interest, all three examples of 3-D printed thru lines exhibit high dissipative attenuation. Our earlier work resulted in a band-average α'_D of 440 dB/m, using a PolyJet printer [12]. It will be shown that our new MSLA printer can achieve 157 dB/m. By comparison, the COTS thru line has a worst-case value of 61 dB/m [16], while the band-average α'_D is 199 dB/m for metal-based printing [19].

B. BANDPASS FILTERS

We have previously reported a detailed literature survey of sub-THz 3-D printed waveguide bandpass filters [11]. At these frequencies, the range of all available manufacturing technologies is limited. The small internal dimensions associated with BPFs reach the limits for most low-cost manufacturing technologies. Moreover, the thin coupling irises are delicate. As a result, only a few examples of sub-THz MPRWG BPFs have been reported in open literature [2], [5], [10], [11], [14]. In general, these filters show more significant center frequency shifting and changes in bandwidth, when compared to those operating at lower-millimeter-wave frequencies (30 to ca. 100 GHz). This highlights the significant challenge for (sub-)THz frequencies, due to the relatively poor manufacturing accuracy associated with today's low-cost 3-D printers.

An exhaustive literature survey has been recently undertaken for terahertz 3-D printed MPRWG bandpass filters. To the best of our knowledge, Table 2 summarizes all the MPRWG bandpass filters that have been reported in the open literature. Table 2 represents a frequency extension to the version in our earlier survey [11]. Only two 3-D printed THz MPRWG BPF examples have been previously reported in open literature [3], [4]; both manufactured using metal-based printers (i.e., MLS [3] and 3-D screen printing [4]). Here, f_c and 3 dB FBW represent the measured center frequency and 3 dB fractional bandwidth; IL is the measured minimum insertion loss; Q_L corresponds to the measured loaded quality (Q -)factor defined by the 3 dB bandwidth.

With the 297 GHz filter, the metal powder is stainless steel (SS), which is subsequently electroless-plated with a 3 μm -thick layer of gold, to improve its effective conductivity. The in-band insertion loss varies between 1.1 dB and 2.7 dB, with a 1% frequency downshift, and return loss better than 10 dB. With the 314 GHz filter, this component is sliced into 4 layers, each individually screen printed, and then assembled using the precision alignment holes and additional dowel pins. The minimum insertion loss is 3.0 dB, with a 4.7% frequency upshift, and return loss better than 11 dB. The poor insertion loss is attributed to the tungsten-copper (W-Cu) paste used in the screen printing process, which exhibits a relatively very low effective conductivity, while the large frequency upshift is attributed to shrinkage.

Unlike these metal-based 5th order Chebyshev 300 GHz filters, it will be shown that our polymer-based 3rd order Butterworth 403 GHz filter has an insertion loss of only 1.0 dB, with a 0.25% frequency downshift, and return loss better than 16 dB.

III. DESIGNS

A. THRU LINES

In this work, all the 3-D printed thru lines, resonators and bandpass filters are implemented in standard WR-2.2 metal-pipe rectangular waveguide, having internal cross-sectional dimensions $a \times b$ of 570 $\mu\text{m} \times 285 \mu\text{m}$ [22], and standard compatible flanges [23]. All simulations are undertaken using Ansys High-Frequency Structure Simulator (HFSS) full-wave electromagnetic modeling software. The initial simulations for the thru line have no rounding, perfectly smooth walls and a textbook value of bulk DC conductivity $\sigma_0 = 5.8 \times 10^7$ S/m, which is also the default value for copper in HFSS.

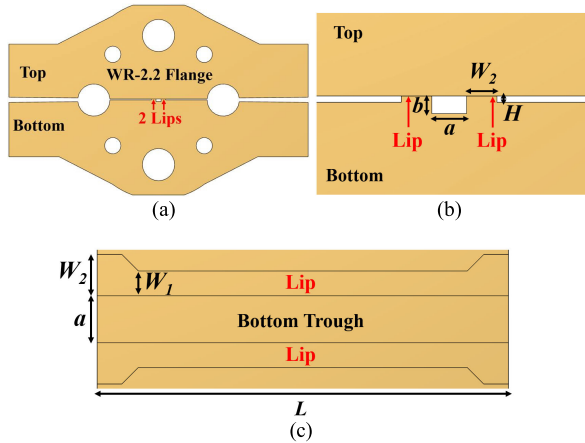


FIGURE 1. Ideal (no rounding) illustrations for our H-plane a -edge split-block WR-2.2 MPRWG thru line: (a) complete flange view; (b) close-in flange view; and (c) plan view of bottom trough.

Our ‘trough-and-lid’ split-block design is chosen to ensure that the plating can provide sufficient metallization at the corners. Conventional symmetric E- and H-plane split-block designs have been previously found to cause misalignment between the two parts [5]. The effects caused by misalignment with 3-D printed MPRWG components are negligible at low frequencies and, therefore, such designs are widely adopted. However, adverse effects become significant at (sub-)THz frequencies. For this reason, an unorthodox H-plane a -edge split is employed here, which avoids misalignment and allows for easier removal of resin residues and visual inspection [11]. As shown in Fig. 1, our split-block design comprises a flat lid top part and trough bottom part. The flat lid allows for slight misalignments in its plane; while two protrusive lips above the trough ensure a good transverse current path between the top and bottom parts, which mitigate against electromagnetic (EM) energy leakage.

Our previous ‘trough-and-lid’ design suffers from rectangular-to-trapezoidal waveguide cross-sectional deformation at the apertures, during initial assembly and flange-to-flange test mating [11]. As a result, a design iteration was required here to ruggedize the lips. The new lip height $H = 100 \mu\text{m}$ (*cf.*, $H = 200 \mu\text{m}$ in our previous work [11]). The previous work for G-band has $550 \mu\text{m}$ wide lips. However, with the smaller WR-2.2 band aperture, the internal lip width is now $W_1 = 300 \mu\text{m}$, which broadens out to $W_2 = 500 \mu\text{m}$ at the aperture. This provides enhanced mechanical strength when the top and bottom parts are assembled and flange-to-flange test mating is undertaken. These empirical lip values seem to be (near-)optimal for the WR-2.2 band; with all values reduced for higher frequency bands.

B. SINGLE-CAVITY RESONATORS

In order to evaluate the adverse effects from manufacturing defects for MPRWG filters, single-cavity resonators are investigated. To this end, the 399 GHz cavity resonators at the center of our 3rd order Butterworth and Chebyshev 403 GHz

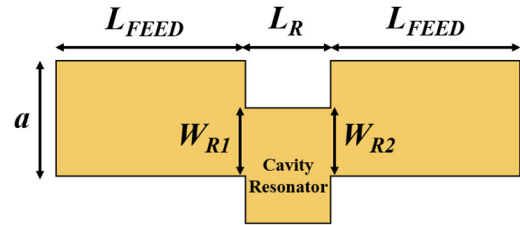


FIGURE 2. Plan view illustration showing internal variable dimensions for an ideal (no rounding) MPRWG single-cavity resonator.

filters are chosen; having a 3 dB FBW of $\sim 14\%$ (56 GHz) and $\sim 13\%$ (54 GHz), respectively. Filter design details are given in Subsection III-C. Figure 2 illustrates the internal variable dimensions for an ideal (no rounding) MPRWG single-cavity resonator.

L_{FEED} represents the feed length to/from the input and output ports; L_R is the cavity resonator length; W_{R1} and W_{R2} correspond to the iris gap widths. With MPRWG filters, conventional diaphragm irises [11] require extremely-high dimensional tolerance manufacturing technologies and with high strength materials – not inherently compatible with low-cost polymer-based 3-D printing. In this work, all resonators are inductively coupled with transverse offset waveguides, while their width dimension has a constant value a [10].

As given in Subsection III-C, the corresponding center resonator design dimensions for the ideal (no rounding) Butterworth and Chebyshev filters are listed in Table 3.

TABLE 3. 399 GHz center resonator design (HFSS simulated) dimensions associated with the ideal (no rounding) and CRC (rounding) Butterworth and Chebyshev 403 GHz filters (with smooth walls and $\sigma_0 = 5.8 \times 10^7 \text{ S/m}$).

Parameter	Butterworth			Chebyshev		
	Ideal (μm)	CRC (μm)	Δ (μm)	Ideal (μm)	CRC (μm)	Δ (μm)
L_{FEED}	2,295	2,296	1	2,293	2,294	1
L_R	411	408	3	415	413	2
$W_{R1} = W_{R2}$	306	297‡	9	300	289‡	11

‡ Chitubox automatically chooses one less pixel for the rounding case.

Iris corner rounding, due to manufacturing imperfections (e.g. with 3-D printing [11]), has a significant effect on the resonance frequency and bandwidth for a single resonator. As a result, it may be necessary to apply appropriate compensation during the design phase in order to mitigate against this effect [11]. Figure 3 shows a plan view microphotograph of the bottom part for single-cavity resonator (after copper plating), showing significant iris corner rounding. Here, $R_{in} = 75 \mu\text{m}$ is the measured average inner corner rounding radius and $R_{out} = 34 \mu\text{m}$ is the measured average outer corner rounding radius. While the former is numerically larger, the latter has the dominant effect (on the coupling coefficients for the resonator). These values are subsequently used in the following corner rounding compensation process.

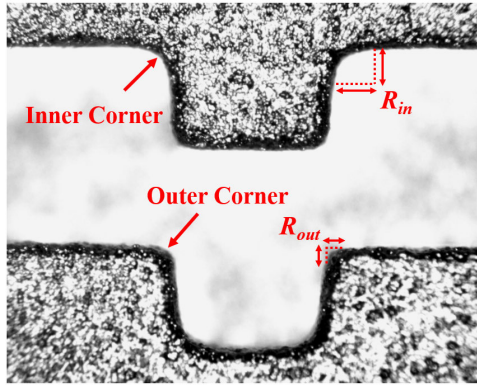


FIGURE 3. Plan view microphotograph of the bottom part for a single-cavity resonator, MSLA 3-D printed with a pixel resolution of $22\ \mu\text{m}$, showing iris corner rounding (after copper plating).

Figure 4 shows the CRC simulation results (with corner rounding, smooth walls and $\sigma_0 = 5.8 \times 10^7\ \text{S/m}$) for the center resonators associated with the Butterworth and Chebyshev filters. The yellow solid line, red solid line, and blue dashed line represent the ideal single-cavity resonator without rounding, rounded before compensation and rounded after compensation, respectively. The yellow and blue arrows indicate frequency shifting of the transmission responses due to detuning and its compensation, respectively. It can be seen that the level of corner rounding, with our MSLA 3-D printer, causes a 1.3% frequency downshift and a 35% increase in the 3 dB bandwidth, due to an increase in both the cavity's effective electrical length and coupling coefficients. By fine-tuning the values of L_R , W_{R1} and W_{R2} in HFSS (using our pre-determined measured values for R_{in} and R_{out}), the compensated rounded resonator shows a very close-fit to the ideal non-rounded case.

Table 3 also gives the center resonator design dimensions for the compensated rounded Butterworth and Chebyshev filters (with smooth walls and $\sigma_0 = 5.8 \times 10^7\ \text{S/m}$). It can be seen that the designed dimensions for two center resonators are very similar. In practice, considering the $22\ \mu\text{m}$ pixel resolution for our MSLA 3-D printer, these two resonators would be printed with exactly the same dimensions – defined by the level of quantization [10]. As a result, only one resonator is needed and chosen as a reference benchmark for investigation.

C. BANDPASS FILTERS

To limit the number of unknowns, when investigating the adverse effects of manufacturing errors on MPRWG filters, we deliberately chose to investigate low (3rd) order filters. For the Chebyshev BPF, the worst-case passband return loss level is designed as 25 dB. Figure 5 shows the internal dimensions for an ideal (no rounding) filter. L_{Fi} ($i \in [1, 2, 3]$) represents the cavity length for the i^{th} cavity and W_{Fi} ($i \in [1, 2, 3, 4]$) is the associated iris gap width.

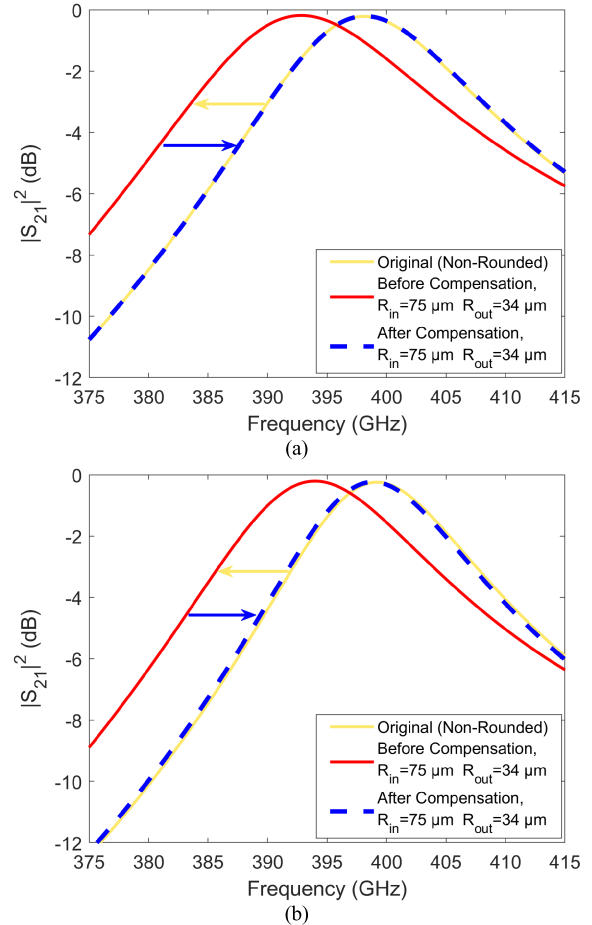


FIGURE 4. CRC simulations (with corner rounding, smooth walls and $\sigma_0 = 5.8 \times 10^7\ \text{S/m}$) for the single-cavity resonators, with yellow and blue arrows indicating frequency shifting due to detuning and its compensation, respectively, with the center resonators for the: (a) Butterworth filter; and (b) Chebyshev filter.

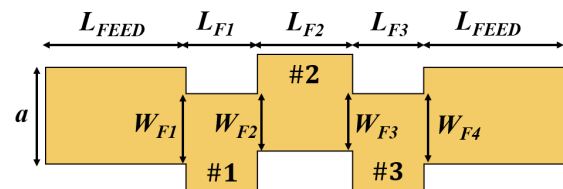


FIGURE 5. Plan view illustration showing internal variable dimensions for an ideal (no rounding) 3rd order MPRWG bandpass filter.

Following standard coupling matrix theory [24], with a filter order $N = 3$, two $(N + 2) \times (N + 2) = [5 \times 5]$ prototype coupling matrices for our target Butterworth M_B and Chebyshev M_C filters, respectively, are extracted and given as:

$$M_B = \begin{bmatrix} 0 & 1 & 0 & 0 & 0 \\ 1 & 0 & 0.7071 & 0 & 0 \\ 0 & 0.7071 & 0 & 0.7071 & 0 \\ 0 & 0 & 0.7071 & 0 & 1 \\ 0 & 0 & 0 & 1 & 0 \end{bmatrix} \quad (1)$$

TABLE 4. Design (HFSS simulated) dimensions for the ideal (no rounding) and CRC (rounding) for Butterworth and Chebyshev filters (with smooth walls and $\sigma_0 = 5.8 \times 10^7$ S/m).

Parameter	Butterworth			Chebyshev		
	Ideal (μm)	CRC (μm)	Δ (μm)	Ideal (μm)	CRC (μm)	Δ (μm)
L_{FEED}	1,937	1,941	4	1,923	1,927	4
$L_{F1} = L_{F3}$	358	355	3	370	367	3
L_{F2}	411	408	3	415	413	2
$W_{F1} = W_{F4}$	395	386	9	375	366	9
$W_{F2} = W_{F3}$	306	297	9	300	289	11

$$M_C = \begin{bmatrix} 0 & 1.2214 & 0 & 0 & 0 \\ 1.2214 & 0 & 1.2197 & 0 & 0 \\ 0 & 1.2197 & 0 & 1.2197 & 0 \\ 0 & 0 & 1.2197 & 0 & 1.2214 \\ 0 & 0 & 0 & 1.2214 & 0 \end{bmatrix} \quad (2)$$

HFSS simulations are undertaken to optimize the filter geometry and the final design dimensions for the ideal (no rounding) 3rd order Butterworth and Chebyshev filters (with smooth walls and $\sigma_0 = 5.8 \times 10^7$ S/m) are given in Table 4.

For the final filter designs, CRC is applied (with smooth walls and $\sigma_0 = 5.8 \times 10^7$ S/m), based on the same pre-determined values for R_{in} and R_{out} . The corresponding EM simulation results are given in Fig. 6.

Table 4 also gives the design dimensions for the compensated rounded 3rd order Butterworth and Chebyshev filters (with smooth walls and $\sigma_0 = 5.8 \times 10^7$ S/m). By comparing the designed dimensions for the resonators (Table 3) and BPFs (Table 4), with and without CRC, with difference $\Delta \leq 11 \mu\text{m}$, it is clear that the $22 \mu\text{m}$ pixel resolution of our 3-D printer is not capable of meeting the target CRC requirements and, thus, CRC is not applied to our BPFs. However, CRC is applied to the resonator, to highlight the problem of overcompensation.

IV. FABRICATION

A. 3-D PRINTING

In this work, all 3-D drawings are undertaken using the computer-aided design (CAD) drawing package Autodesk Fusion 360 [25]. The output drawing file, having the standard tessellation language (STL) format, is imported into the slicing software Chitobox [26]. Here, the Phrozen Sonic Mini 8K MSLA 3-D printer is used, with a quoted print volume of $165 \text{ mm} \times 72 \text{ mm} \times 180 \text{ mm}$. As stated previously, the pixel resolution on the x - y build plane is quoted to be $22 \mu\text{m}$, although this will degrade over time, and the default vertical layer thickness on the z -axis can range from 10 to $300 \mu\text{m}$ [27].

With our MSLA printer, the Elegoo water washable photopolymer resin (Ceramic Grey) was used; mainly for its high precision, low shrinkage and ease of post-processing.

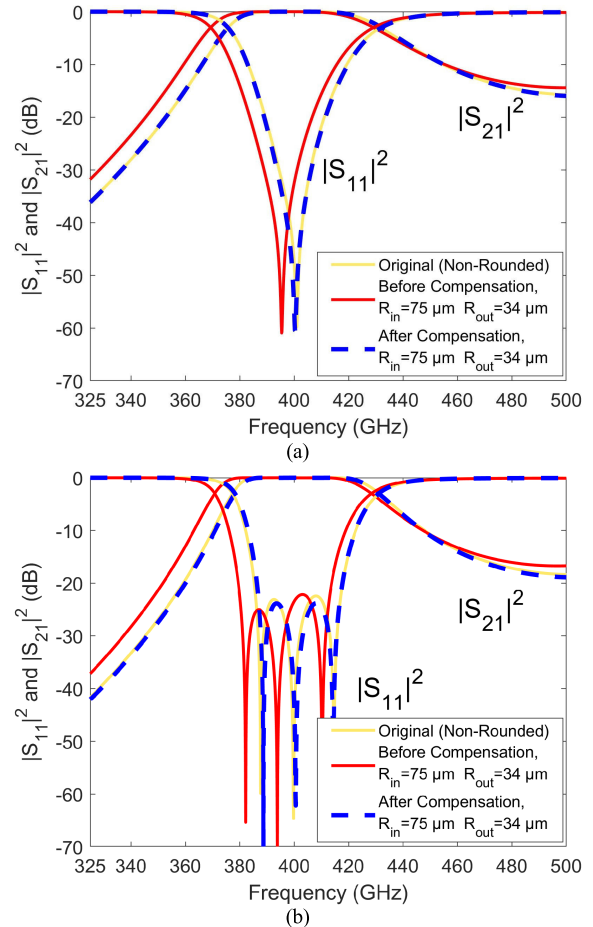


FIGURE 6. CRC simulations (with smooth walls and $\sigma_0 = 5.8 \times 10^7$ S/m) for the 3rd order 403 GHz filters: (a) Butterworth filter; and (b) Chebyshev filter.

B. METALIZATION

Visual inspection (under a microscope) of the 3-D printed parts is necessary to remove those with any signs of manufacturing defects. The remaining parts are then copper plated using a commercial process. Here, a thin layer of nickel is first electroless-plated onto the 3-D printed part surfaces; this is then followed by electroplating a $5 \mu\text{m}$ thick layer of copper. Finally, the plated parts are processed with a proprietary anti-tarnishing treatment.

Scanning electron microscope (SEM) images for a thru line and a 3rd order BPF are shown in Figs. 7(a) and 7(b), respectively. Figure 7(c) shows the close-in flange view of the bottom part of the BPF. The ceiling rounding radius has a measured average value $R_c = 34 \mu\text{m}$. A close-in plan view of the bottom trough surface roughness is shown in Fig. 7(d).

After copper plating, the two parts are assembled for testing. Figure 8 shows photographs of an H-plane split-block WR-2.2 3rd order Chebyshev MPRWG BPF before and after assembly. The black circular holes show where 1.5 mm diameter and 5.0 mm long stainless-steel dowel pins are inserted, to provide alignment.

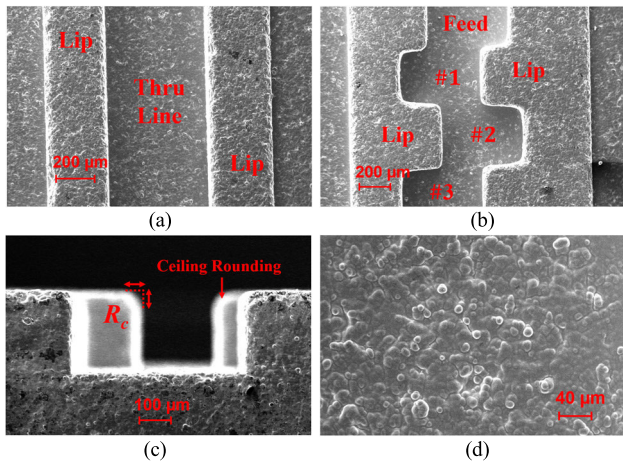


FIGURE 7. SEM images for 3-D printed MPRWG components (after copper plating): (a) thru line; (b) 3rd order Chebyshev filter; (c) close-in flange view of the bottom part of the filter; and (d) close-in plan view of the bottom trough surface.

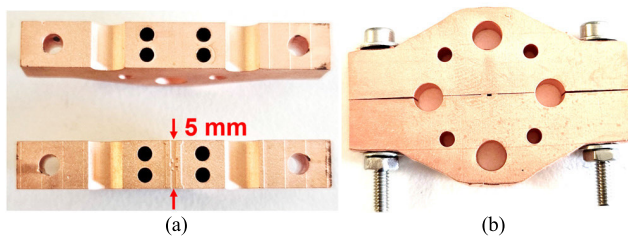


FIGURE 8. Photographs of a 3-D printed H-plane split-block WR-2.2 3rd order Chebyshev filter (after copper plating): (a) disassembled; and (b) assembled.

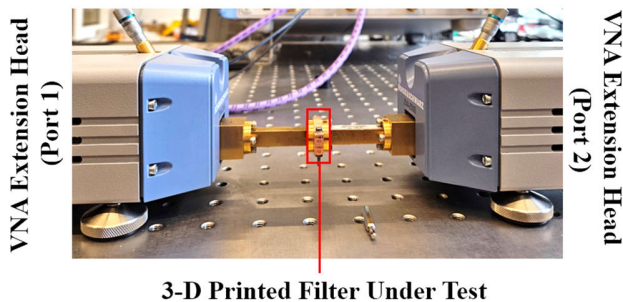


FIGURE 9. Typical measurement setup for 3-D printed MPRWG components (after copper plating).

V. MEASUREMENTS

Scattering (S-)parameter measurements were undertaken within the Department of Materials at Imperial College London, using their Rohde & Schwarz ZVA 67 vector network analyzer and ZVA-Z500 frequency extension heads. The typical measurement setup for 3-D printed MPRWG components is shown in Fig. 9.

For our two-port S-parameter measurements in waveguide, at submillimeter-wave frequencies, the Thru-Reflect-Line (TRL) calibration scheme was adopted [28]. This choice offers the advantage of requiring only partial

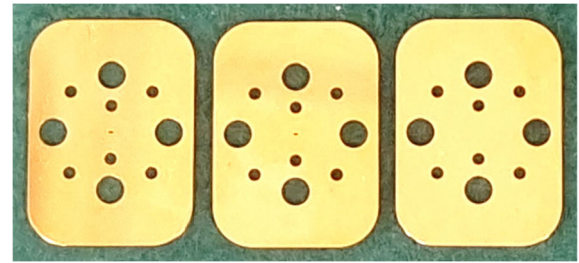


FIGURE 10. National Physical Laboratory's WR-2.2 band $\frac{3}{4}$ -wave TRL waveguide calibration standards: lower-band, longer Line (left); upper-band shorter Line (center); flush short Reflect (right).

information regarding the calibration standards. Specifically, TRL requires identical Reflect standards at both waveguide test ports, and the Line standard with the correct waveguide aperture dimensions.

Traditionally, the TRL calibration scheme employs a Line standard having a 90° electrical length (equivalent to a quarter-guided wavelength) at the midband frequency; this allows the transmission phase change to range between approximately 30° and 150° over the frequency range of interest within the band. However, at submillimeter-wave frequencies, the use of $\frac{1}{4}$ -wave Line standards becomes problematic, due to their very short physical length (i.e., <250 μm for the WR-2.2 band), leading to mechanical integrity issues.

For this reason, as an alternative approach, our TRL calibration employed $\frac{3}{4}$ -wave Line standards, which allow transmission phase changes to range between 210° and 330° over the frequency range of interest within the band. These waveguides are significantly more mechanically robust, due to their increased thickness [29]. For this purpose, two Line standards were employed, both manufactured by SWISSto12. The first Line standard has a designed physical length of 951 μm, covering the lower frequency range of the WR-2.2 band (from 325 GHz to 394 GHz); while the second Line standard has a designed physical length of 651 μm, covering the higher frequency range (from 380 GHz to 500 GHz).

A flush short, also manufactured by SWISSto12, was used as the Reflect standard for both of the waveguide test ports. The calibration standards employed for these measurements are shown in Fig. 10. The S-parameter measurement results created using both $\frac{3}{4}$ -wave Line standards were combined using the weighting scheme [29], to achieve a full-band calibration.

A. THRU LINE

Figure 11 shows the simulated, re-simulated and measured S-parameter results for the 5 mm-long thru line. As can be seen in Fig. 11(a), the measured return loss is better than 13.3 dB across the WR-2.2 band. The worst-case measured insertion loss is 1.2 dB at the lower band-edge frequency of 325 GHz, 0.8 dB at 400 GHz and 0.4 dB at the upper band-edge frequency of 500 GHz. The average insertion loss across the whole band is 0.9 dB.

According to initial HFSS simulations, where the default value of effective conductivity is used, there is no significant effect caused by ceiling rounding, with insertion loss degraded by less than 0.1 dB, which is well within experimental error at these frequencies. However, corner rounding will cause filter center frequency shifting and increased bandwidth, but without introducing significant insertion loss.

In all HFSS re-simulations, both ceiling and corner rounding are included to represent our practical scenario. The physical dimensions associated with our thru line, single-cavity resonators and filters are measured individually, and these dimensions are then incorporated into HFSS re-simulations. In addition, as will be discussed later in this Subsection, the effective conductivity is reduced from the default value to 0.36×10^7 S/m. From Fig. 11(a), the re-simulated S-parameter responses for the thru line match very closely with the measurements.

Assuming a perfect wave impedance match at both test ports (which is not a bad approximation, given the good measured return loss performance), the ideal transmittance $|S_{21}|^2$ and its corresponding insertion loss $IL|_{Ideal}$ for an air-filled MPRWG thru line are given as:

$$|S_{21}|^2 = e^{-2\alpha_c L} \tag{3}$$

$$IL|_{Ideal} \cong 8.686\alpha_c L \text{ [dB]} \tag{4}$$

$$\alpha_c = \frac{R_S}{\eta_0} \cdot \frac{2\pi^2 b + a^3 k_0^2}{a^3 b \beta k_0} \text{ [Np/m]} \tag{5}$$

where, S_{21} , α_c , $\beta = 2\pi/\lambda_g$, λ_g , k_0 , η_0 and R_S are the respective forward voltage-wave transmission coefficient, attenuation constant associated with the smooth conductor [30], phase constant, guided wavelength, modified wavenumber in free space, intrinsic impedance of free space and surface impedance of the conductor.

The total power attenuation $\alpha_T = \alpha_M + L\alpha'_D = -10 \log_{10} |S_{21}|^2$ is equal to insertion loss, where, α_M represents the contribution to the total attenuation due to the wave impedance mismatch reflection at the input port and α'_D represents the dissipative attenuation per unit length due to ohmic losses and any leakage radiation [5], [11], [31]:

$$\alpha_M = -10 \log_{10} (1 - |S_{11}|^2) \text{ [dB]} \tag{6}$$

$$\alpha'_D = -\frac{10}{L} \log_{10} \left(\frac{|S_{21}|^2}{1 - |S_{11}|^2} \right) \text{ [dB/m]} \tag{7}$$

where, S_{11} is the input voltage-wave reflection coefficient.

With general surface roughness models, roughness coefficient K is used to normalize either the power dissipated P_{DR} or dissipative attenuation α'_{DR} for rough conductors to those for smooth conductors (P_{DS} and α'_{DS}), with [11] and [32]:

$$K = \frac{P_{DR}}{P_{DS}} = \frac{\alpha'_{DR}}{\alpha'_{DS}} \tag{8}$$

In this work, two surface roughness models (i.e., the Extended- and Huray-Hemispherical models [11]) are used in the HFSS re-simulations. According to the SEM image

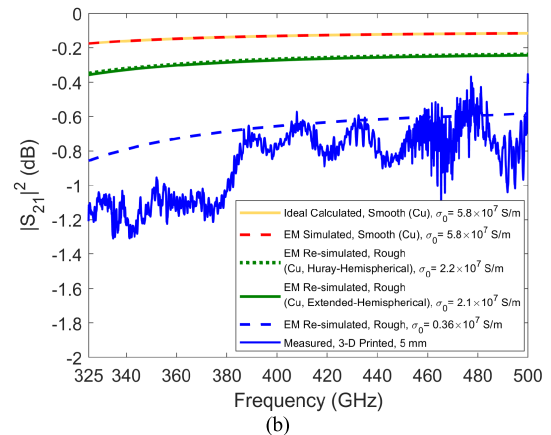
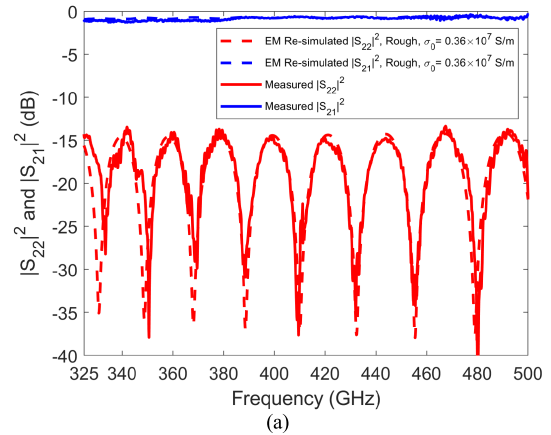


FIGURE 11. Simulated (with no rounding, smooth walls and $\sigma_0 = 5.8 \times 10^7$ S/m), re-simulated (with full rounding, smooth walls and $\sigma_0 = 0.36 \times 10^7$ S/m) and measured S-parameters for the 3-D printed 5 mm-long thru line: (a) $|S_{22}|^2$ and $|S_{21}|^2$; and (b) close-in $|S_{21}|^2$.

in Fig. 7(d), the measured average hemispherical radius r_{base} and separation distance between adjacent protrusions d_{peaks} are $4.7 \mu\text{m}$ and $14.8 \mu\text{m}$, respectively; this is commensurate with our respective previous measured values of $3.7 \mu\text{m}$ and $17 \mu\text{m}$ [11]. The calculated roughness coefficients at 400 GHz are $K(400\text{GHz}) = 1.66$ and 1.62 for the Extended- and Huray-Hemispherical models, with the associated effective conductivity of 2.1×10^7 S/m and 2.2×10^7 S/m, respectively. As expected, these are greater than those of $K(180\text{GHz}) = 1.32$ and 1.28 , previously found at G-band [11].

The HFSS re-simulated results that include the two surface roughness models are shown in Fig. 11(b), as solid and dashed green lines. It can be seen that there is a large discrepancy between the re-simulated and measured results. It is believed that, in addition to surface roughness, there may be a loss contribution due to contact resistance between the two parts of our H-plane a -edge split-block assembly. However, the anti-tarnishing coating applied to the copper surface is the dominant contributor to the measured dissipative attenuation (which further lowers the effective conductivity) at terahertz frequencies; this coating is not included in either of the

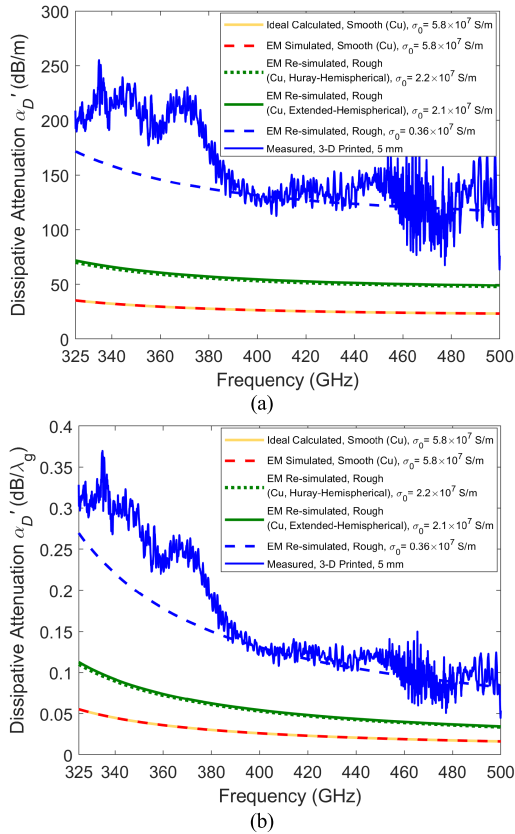


FIGURE 12. Simulated (with no rounding, smooth walls and $\sigma_0 = 5.8 \times 10^7$ S/m), re-simulated (with full rounding, smooth walls and $\sigma_0 = 0.36 \times 10^7$ S/m) and measured dissipative attenuation for the 3-D printed 5 mm-long thru line: (a) per meter; and (b) per guided wavelength.

surface roughness models. Figure 12 shows the simulated, re-simulated and measured dissipative attenuation for the thru line. For WR-2.2, our measured average dissipative attenuation is 157 dB/m and 0.16 dB/ λ_g .

B. SINGLE-CAVITY RESONATORS

Figures 13(a) and 13(b) show the simulated, re-simulated and measured S-parameter responses for the 3-D printed single-cavity resonators without and with CRC, respectively. In Fig. 13(a), the measured resonance frequency f_{0c} for the resonator without CRC is 390.0 GHz, with 2.3% (9.2 GHz) downshift from the ideal simulated resonance frequency $f_{0cn} = 399.2$ GHz. The measured 3 dB bandwidth $\Delta f_{3dB} = 27.1$ GHz, having an increase of 66.3% (10.8 GHz) from the ideal simulation of 16.3 GHz.

As discussed in Section III, corner rounding can cause resonance frequency downshifting and an increase in bandwidth. Therefore, the discrepancies found between the original simulated and measured results are mainly due to corner rounding. As shown in Fig. 13(b), the measured resonance frequency for the resonator with CRC is 407.9 GHz, with 2.2% (8.7 GHz) upshift from the ideal simulated resonance

frequency $f_{0cn} = 399.2$ GHz. The measured 3 dB bandwidth $\Delta f_{3dB} = 18.5$ GHz, having an increase of 13.5% (2.2 GHz) from the ideal simulation of 16.3 GHz. Here, there is a significant reduction in the bandwidth error with the use of CRC. The upshift in resonance frequency is mainly due to Chitubox automatically reducing the width of the resonator by one pixel for our Phrozen 3-D printer, having a 22 μm pixel resolution, when compared to the required value ($\Delta \sim 10$ μm , given in Table 3) resulting in overcompensation in this case.

As we demonstrated previously [11], emulated time-domain reflectometry (TDR) is a useful tool. TDR measurements for the 5 mm-long thru line and single-cavity resonator, without CRC, have been undertaken and the results are shown in Fig. 14. The physical distance d between any two points on a TDR trace is given by [11] and [33]:

$$d \simeq v_g \Delta t / 2 \quad (9)$$

where, v_g is the group velocity of the MPRWG and Δt represents the round-trip time difference between any two points on the trace.

For our thru line, the measured Δt between blue peaks #1 and #2 is 45.7 ps. With group velocity $v_g \sim v_g(400 \text{ GHz}) \simeq 2.26 \times 10^8$ m/s, this corresponds to the waveguide flange-to-flange physical length $d = 5,164$ μm , with only 3.3% error, when compared to the design value for $L = 5,000$ μm . For the single-cavity resonator, the measured Δt between red peaks #1 and #2 is 20.6 ps. This corresponds to the waveguide feed length $d = 2,328$ μm , with only 1.4% error, which matches very closely with our design value for $L_{FEED} = 2,295$ μm .

Figure 15 shows the RLC equivalent circuit model for any undriven resonator (i.e., uncoupled to any source or load impedances). With a lossy scenario, the associated complex natural angular (or eigen)frequency is related to the resonator unloaded Q -factor $Q_U(\omega_0)$ as follows [34]:

$$\tilde{\omega}_0 = \omega_0 \left[\sqrt{1 - \left(\frac{1}{2Q_U(\omega_0)} \right)^2} + j \frac{1}{2Q_U(\omega_0)} \right] \equiv \omega'_0 + j\omega''_0 \quad (10)$$

where, $\omega_0 = |\tilde{\omega}_0| = 2\pi f_0$ is the driven angular resonance frequency, $f_0 = 1/2\pi \sqrt{L(\omega_0)C(\omega_0)}$ is the driven resonance frequency; ω'_0 is the damped (or undriven) natural angular resonance frequency; and ω''_0 is the field (amplitude) decay rate or Napier frequency.

For any air-filled cavity resonator, the exact RLC parameter values can be extracted from [34]:

$$R(\tilde{\omega}_0) = 2\omega''_0 L(\omega_0) \quad (11)$$

$$L(\omega_0) = \mu_0 V \left(\frac{\omega_0}{c} \right)^2 \quad (12)$$

$$C(\omega_0) = \frac{\epsilon_0}{V} \left(\frac{c}{\omega_0} \right)^4 \quad (13)$$

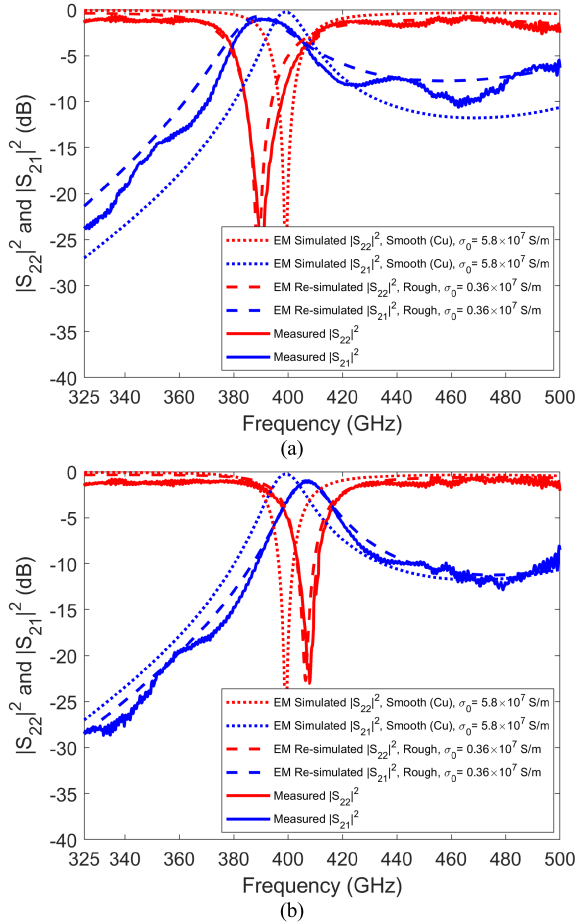


FIGURE 13. Simulated (with no rounding, smooth walls and $\sigma_0 = 5.8 \times 10^7$ S/m), re-simulated (with full rounding, smooth walls and $\sigma_0 = 0.36 \times 10^7$ S/m) and measured S-parameters for the 3-D printed 5 mm-long 399 GHz single-cavity resonators: (a) without CRC; and (b) with CRC.

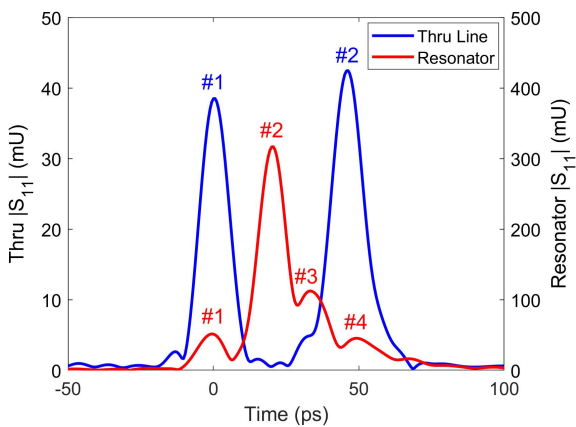


FIGURE 14. Emulated TDR measurement results: (a) thru line, extracted from Fig. 10(a); and (b) 399 GHz resonator, without CRC, extracted from Fig. 12(a).

where, $c = 1/\sqrt{\epsilon_0\mu_0}$, ϵ_0 and μ_0 are the speed of light, permittivity and permeability, all in free space; V is the volume of the cavity resonator – for example, $V = 0.06677$ mm³ for the center resonator of the ideal simulated Butterworth

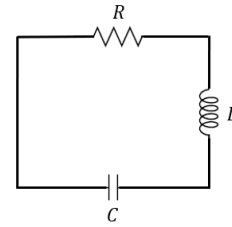


FIGURE 15. RLC equivalent circuit model for an undriven resonator that is uncoupled to any source or load.

TABLE 5. Measurement extracted normalized values of $Q_L(f_{0c})$, $Q_U(f_0)$, and RCL elements for the cavity resonators.

CRC	f_{0c}/f_{0cn}	$Q_L(f_{0c})/Q_{Ln}(f_{0cn})$	f_0/f_{0n}	$Q_U(f_0)/Q_{Un}(f_{0n})$	R/R_n	L/L_n	C/C_n
No	0.98	0.59	0.99	0.15	5.36	0.83	1.22
Yes	1.02	0.90	1.01	0.24	3.57	0.84	1.18

filter ($V = 0.06742$ mm³ for the Chebyshev filter), using the values from Table 3.

Given that the cavity resonator is EM-coupled to both a source and load, both ideally having the same wave impedance (defined by the MPRWG), the new driven resonance frequency $f_{0c} < f_0$. At this point, it is important to state that the unloaded Q -factor $Q_U(f_0)$ is replaced by $Q_U(f_{0c}) = Q_U(f_0) \cdot f_{0c}/f_0 < Q_U(f_0)$. The extracted loaded quality factor $Q_L(f_{0c})$ and unloaded quality factor $Q_U(f_{0c})$ for the resonator are given as [5], [24], and [30]:

$$Q_L(f_{0c}) = \frac{f_{0c}}{\Delta f_{3dB}} \quad (14)$$

$$Q_U(f_{0c}) = \frac{Q_L(f_{0c})}{1 - |S_{21}(f_{0c})|} \quad (15)$$

Using (11)-(15), the associated RLC elements for the cavity resonators can be extracted from measurements of f_{0c} , Δf_{3dB} and $|S_{21}(f_{0c})|$, with the results shown in Table 5. Here, the ideal simulated cavity resonator represents the reference benchmark (with no rounding, smooth walls and $\sigma_0 = 5.8 \times 10^7$ S/m), and all these parameters are depicted with subscript n . HFSS frequency-domain simulations give values for $f_{0cn} = 399.2$ GHz, $\Delta f_{3dBn} = 16.3$ GHz and, $|S_{21n}(f_{0cn})| = 0.97$; giving $Q_{Ln}(f_{0cn}) = 24.5$ using (14), and $Q_{Un}(f_{0cn}) = 863.2$ using (15). Using the linear relationship $Q_{Un}(f_{0cn}) = Q_{Un}(f_{0n}) \cdot f_{0cn}/f_{0n}$ with $f_{0n} = 446.6$ GHz extracted from the HFSS eigenmode solver gives $Q_{Un}(f_{0n}) = 965.7$. As a result, using (11) to (13), the benchmark RLC element values are $R_n = 21.6 \Omega$, $L_n = 7.4$ nH and $C_n = 17.1$ aF.

When compared to the reference benchmark (ideal simulations), the measured cavity resonator without CRC exhibits a significant decrease of 41% in $Q_L(f_{0c})$. This is due to resonance frequency downshifting and an increase in its bandwidth (mainly caused by corner rounding). After applying CRC, there is an obvious improvement in $Q_L(f_{0c})$, with a decrease of only 10% from the ideal simulated value. Both

resonators (without and with CRC) suffer from relatively low values of $Q_U(f_0)$, mainly due to the high resistance R that is attributed to the low effective conductivity. Moreover, when compared to the reference benchmark, both resonators exhibit $\sim 17\%$ decrease in the inductance L and $\sim 20\%$ increase in capacitance C ; with negligible net change in f_{0c} and f_0 .

C. BANDPASS FILTERS

Figure 16 shows the simulated, re-simulated and measured S-parameter responses for the 3-D printed 3rd order Butterworth and Chebyshev BPFs. Note that both MPRWG filters are designed without CRC; as previously stated, the resolution of our 3-D printer is not capable of meeting the target CRC requirements.

As shown in Fig. 16(a), the measured and re-simulated S-parameter responses for the 3rd order Butterworth BPF do not attain the typical Butterworth approximation. This is mainly due to resonator detuning, caused by dimensional inaccuracies during manufacturing. The measured center frequency for this filter is 406.1 GHz, with its measured worst-case return loss of 16.6 dB and 3 dB bandwidth of 64.2 GHz. At center frequency, the measured insertion losses for the 5 mm filter and 5 mm reference thru line are 0.95 dB and 0.68 dB, respectively, having a discrepancy of only 0.27 dB at 406.1 GHz. When compared to the HFSS simulations, with ideal design dimensions given in Table 4, there is a slight center frequency upshift of 0.8% (3.4 GHz) and an increase of 14.2% (8 GHz) in 3 dB bandwidth, with a decrease in loaded quality factor from the simulated value of 7.2 to the measured value of 6.3.

As shown in Fig. 16(b), the measured and re-simulated S-parameter responses for the 3rd order Chebyshev BPF attain the typical characteristic return loss zero distribution. The measured center frequency for this filter is 398.6 GHz, with its measured worst-case return loss of 10.4 dB and 3 dB bandwidth of 65.2 GHz. At center frequency, the measured insertion losses for the 5 mm filter and 5 mm reference thru line are 1.02 dB and 0.83 dB, respectively, having a discrepancy of only 0.19 dB at 398.6 GHz. When compared to the HFSS simulations, with ideal design dimensions given in Table 4, there is a slight center frequency downshift of 1.2% (4.8 GHz) and an increase of 20.7% (11.2 GHz) in 3 dB bandwidth, with a decrease in loaded quality factor from the simulated value of 7.5 to the measured value of 6.1.

With both filters, the increase in 3 dB bandwidth is mainly due to corner rounding and dimensional errors increasing the iris gap widths; both increasing the coupling coefficients associated with the cavity resonators. When compared to the ideal design simulation responses, the additional measured insertion loss is mainly attributed to the surface roughness and the anti-tarnishing coating on the copper surface, which reduce the total effective conductivity. When compared to the Chebyshev counterpart, it is clear that the Butterworth filter is more robust against manufacturing errors, in terms

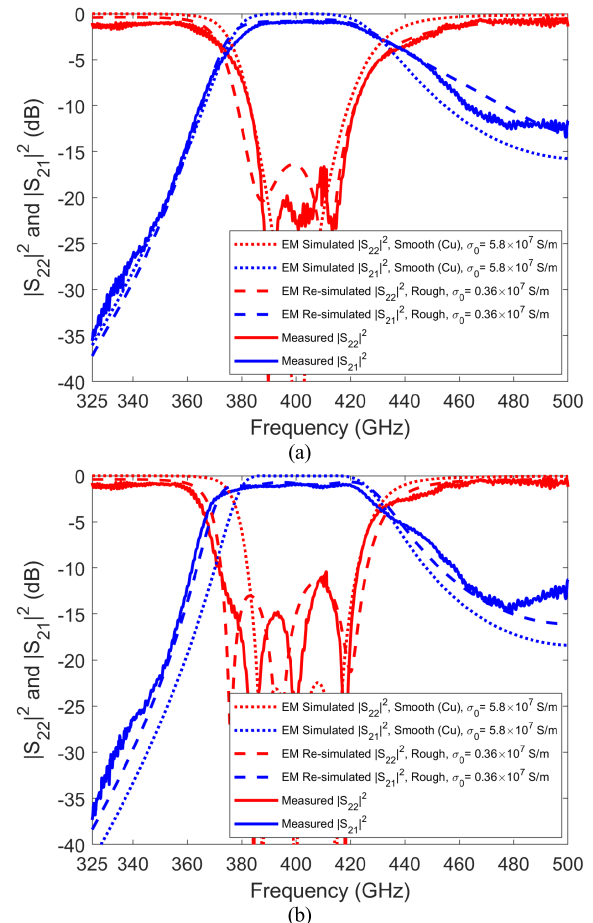


FIGURE 16. Simulated (with no rounding, smooth walls and $\sigma_0 = 5.8 \times 10^7$ S/m), re-simulated (with full rounding, smooth walls and $\sigma_0 = 0.36 \times 10^7$ S/m) and measured S-parameters for the 3-D printed 5 mm-long 3rd order 403 GHz filters: (a) Butterworth; and (b) Chebyshev.

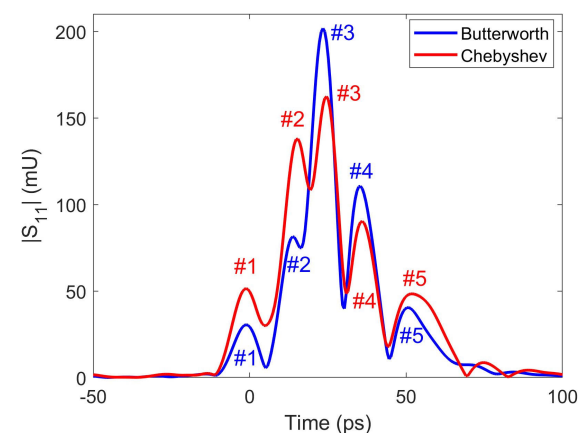


FIGURE 17. Emulated TDR measurement results for the 3-D printed Butterworth and Chebyshev 403 GHz filters.

of absolute frequency shift, insertion loss and worst-case return loss.

Emulated TDR measurements for the 5 mm-long 3-D printed Butterworth and Chebyshev filters have been

undertaken and the results are shown in Fig. 17. For the Butterworth filter, the measured Δt between blue peaks #1 and #2 is 16.6 ps. This corresponds to the waveguide feed length $d = 1,876 \mu\text{m}$, with only 3.1% error, which matches closely with our design value for $L_{FEED} = 1,937 \mu\text{m}$. For the Chebyshev filter, the measured Δt between red peaks #1 and #2 is 17.3 ps. This corresponds to the waveguide feed length $d = 1,955 \mu\text{m}$, with only 1.7% error, which matches very closely with our design value for $L_{FEED} = 1,923 \mu\text{m}$.

The Chebyshev filter exhibits better defined reflections, when compared to the Butterworth filter. With reference to the blue and red #1 peaks, the weaker reflection demonstrated by the Butterworth filter is indicative of a better input impedance match, when compared to the Chebyshev filter. With reference to blue and red #2 peaks, the stronger reflection demonstrated by the Chebyshev filter is indicative of a narrower iris gap width, associated with a lower coupling coefficient from the feed into the first resonator, when compared to the Butterworth filter.

VI. DISCUSSION AND CONCLUSION

This paper presents the state-of-the-art in polymer-based 3-D printing of metal-pipe rectangular waveguides with the first reported terahertz filters.

Unlike metal-based 3-D printing, polymer-based 3-D printing suffers from relatively poor mechanical tolerances, which can result in rectangular-to-trapezoidal waveguide cross-sectional deformation at the apertures; being more pronounced at high frequencies. To this end, a design iteration for our ‘trough-and-lid’ solution was implemented. The more ruggedized lips are (near-)optimal for the WR-2.2 band, but will need to be redesigned for higher frequency bands.

Our 3-D printed thru line has the lowest reported dissipative attenuation of 157 dB/m, when compared to other 3-D printed thru lines at WR-2.2 band, with a measured worst-case return loss of 13.3 dB across the waveguide band. In addition, emulated TDR measurements have been investigated, and this shows negligible physical aberrations (e.g., aperture deformations and re-orientations) at the test-port flange interfaces, insignificant surface defects within the waveguides and no obvious radiation leakage (indicated by excess losses and spurious resonances) from the split block.

Polymer-based 3-D printed waveguide bandpass filters have been demonstrated at terahertz frequencies. The measured insertion losses for these 3rd order Butterworth and Chebyshev filters are only 1 dB at their center frequencies, with the worst-case return losses of 16.6 dB and 10.4 dB, respectively. This shows that the Butterworth filter is more robust against manufacturing errors than its Chebyshev counterpart.

With the single-cavity resonators, corner rounding compensation results in excess frequency shifting of the resonance frequency, indicating that the 22 μm pixel resolution of

our Phrozen MSLA 3-D printer is not sufficient for the dimensional tolerance needed for the WR-2.2 band. For this reason, neither quantization predistortion [10] or corner rounding compensation [11] are employed here for our filters.

With quantization predistortion, dimensional measurement errors dominate when they become commensurate with pixel resolution, and so it is only effective with lower pixel resolution 3-D printers. However, with corner rounding compensation, higher pixel resolution is required (e.g., $<10 \mu\text{m}$ for the WR-2.2 band). The Elegoo Mars 4 has recently come onto the market as a low-cost (currently retailing at \$259) 9K 3-D printer, having an 18 μm pixel resolution on the x - y build plane [35]. Using this 9K printer, it is believed that CRC can be applied to resonators and filters (without causing significant overcompensation) in the WR-3 band and lower frequencies. As pixel sizes continue to shrink, it is believed that THz waveguide components, employing CRC, can be 3-D printed in the near future.

Our latest work opens-up new opportunities for applications where high performance and low manufacturing cost are the main drivers (e.g., future 5G+ mobile communications, radar and imaging systems), which could one day compete with traditional machining technologies.

ACKNOWLEDGMENT

The authors would like to thank W. He for taking the SEM images and Dr. S. Ramadan for arranging the measurements.

REFERENCES

- [1] M. Salek, X. Shang, R. C. Roberts, M. J. Lancaster, F. Boettcher, D. Weber, and T. Starke, “W-band waveguide bandpass filters fabricated by micro laser sintering,” *IEEE Trans. Circuits Syst. II, Exp. Briefs*, vol. 66, no. 1, pp. 61–65, Jan. 2019.
- [2] T. Skaik, M. Salek, Y. Wang, M. Lancaster, T. Starke, and F. Boettcher, “180 GHz waveguide bandpass filter fabricated by 3D printing technology,” in *Proc. 13th U.K.-Eur.-China Workshop Millimetre-Waves THz Technol. (UCMMT)*, Aug. 2020, pp. 1–3.
- [3] T. Skaik, Y. Wang, M. Salek, P. Hunyor, H. Wang, P. G. Huggard, T. Starke, M. Attallah, and R. Martinez, “A 3-D printed 300 GHz waveguide cavity filter by micro laser sintering,” *IEEE Trans. THz Sci. Technol.*, vol. 12, no. 3, pp. 274–281, May 2022.
- [4] T. Skaik, M. Salek, Y. Wang, P. G. Huggard, P. Hunyor, H. Wang, and K. Reuter, “A300 GHz waveguide cavity filter fabricated by 3D screen printing technology,” in *Proc. 52nd Eur. Microw. Conf. (EuMC)*, Sep. 2022, pp. 302–305.
- [5] M. D’Auria, W. J. Otter, J. Hazell, B. T. W. Gillatt, C. Long-Collins, N. M. Ridler, and S. Lucyszyn, “3-D printed metal-pipe rectangular waveguides,” *IEEE Trans. Compon., Packag., Manuf. Technol.*, vol. 5, no. 9, pp. 1339–1349, Sep. 2015.
- [6] S.-H. Shin, D. F. Alyasiri, M. D’Auria, W. J. Otter, C. W. Myant, D. Stokes, Z. Tian, N. M. Ridler, and S. Lucyszyn, “Polymer-based 3-D printed Ku-band steerable phased-array antenna subsystem,” *IEEE Access*, vol. 7, pp. 106662–106673, 2019.
- [7] L. Zhu, I. W. Rossuck, R. Payapulli, S.-H. Shin, and S. Lucyszyn, “3-D printed W-band waveguide twist with integrated filtering,” *IEEE Microw. Wireless Technol. Lett.*, vol. 33, no. 6, pp. 659–662, Jun. 2023.
- [8] L. Zhu, S.-H. Shin, R. Payapulli, T. Machii, M. Motoyoshi, N. Suematsu, N. M. Ridler, and S. Lucyszyn, “3-D printed rectangular waveguide 123–129 GHz packaging for commercial CMOS RFICs,” *IEEE Microw. Wireless Technol. Lett.*, vol. 33, no. 2, pp. 157–160, Feb. 2023.
- [9] S. Lucyszyn, X. Shang, W. J. Otter, C. W. Myant, R. Cheng, and N. M. Ridler, “Polymer-based 3D printed millimeter-wave components for spacecraft payloads,” in *IEEE MTT-S Int. Microw. Symp. Dig.*, Jul. 2018, pp. 1–3.

- [10] L. Zhu, R. Payapulli, S.-H. Shin, M. Stanley, N. M. Ridler, and S. Lucyszyn, "3-D printing quantization predistortion applied to sub-THz chained-function filters," *IEEE Access*, vol. 10, pp. 38944–38963, 2022.
- [11] R. Payapulli, L. Zhu, S.-H. Shin, M. Stanley, N. M. Ridler, and S. Lucyszyn, "Polymer-based 3-D printed 140 to 220 GHz metal waveguide thru lines, twist and filters," *IEEE Access*, vol. 11, pp. 32272–32295, 2023.
- [12] W. J. Otter and S. Lucyszyn, "Hybrid 3-D-printing technology for tunable THz applications," *Proc. IEEE*, vol. 105, no. 4, pp. 756–767, Apr. 2017.
- [13] W. J. Otter, N. M. Ridler, H. Yasukochi, K. Soeda, K. Konishi, J. Yumoto, M. Kuwata-Gonokami, and S. Lucyszyn, "3D printed 1.1 THz waveguides," *Electron. Lett.*, vol. 53, no. 7, pp. 471–473, Mar. 2017.
- [14] S.-H. Shin, R. Payapulli, L. Zhu, M. Stanley, X. Shang, N. M. Ridler, and S. Lucyszyn, "3-D printed plug and play prototyping for low-cost sub-THz subsystems," *IEEE Access*, vol. 10, pp. 41708–41719, 2022.
- [15] S.-H. Shin, X. Shang, N. M. Ridler, and S. Lucyszyn, "Polymer-based 3-D printed 140–220 GHz low-cost quasi-optical components and integrated subsystem assembly," *IEEE Access*, vol. 9, pp. 28020–28038, 2021.
- [16] Flann Microwave. (2022). *Flann Microwave*. Accessed: Jun. 25, 2023 [Online]. Available: <https://flann.com/wp-content/uploads/2022/03/Sub-Millimetre-Seamless-Waveguide-Datasheet-Revision-3.pdf>
- [17] A. von Bieren, E. de Rijk, J.-Ph. Ansermet, and A. Macor, "Monolithic metal-coated plastic components for mm-wave applications," in *Proc. 39th Int. Conf. Infr., Millim., THz waves (IRMMW-THz)*, Sep. 2014, pp. 1–2.
- [18] K. Soeda, K. Naganuma, K. Konishi, H. Tamaru, N. Mio, H. Ito, and J. Yumoto, "3D-printed waveguide for 220 GHz–325 GHz band," in *Proc. 47th Int. Conf. Infr., Millim. THz Waves (IRMMW-THz)*, Aug. 2022, pp. 1–2.
- [19] Z. Wu, G. Shi, Y. Yu, X. Wen, C. Guo, and A. Zhang, "Micro metal additive manufactured low-loss slotted rectangular waveguides operating at 220–500 GHz," *Frontiers Phys.*, vol. 9, pp. 1–7, May 2021, Art. no. 696318.
- [20] B. Zhang and H. Zirath, "Metallic 3-D printed rectangular waveguides for millimeter-wave applications," *IEEE Trans. Compon., Packag., Manuf. Technol.*, vol. 6, no. 5, pp. 796–804, May 2016.
- [21] S. Makhlof, B. Khani, J. Lackmann, S. Dülme, and A. Stöhr, "Metallic 3D printed rectangular waveguides (WR3) for rapid prototyping of THz packages," in *Proc. 1st Int. Workshop Mobile THz Syst. (IWMTS)*, Jul. 2018, pp. 1–4.
- [22] *IEEE Standard for Rectangular Metallic Waveguides and Their Interface for Frequencies of 110 GHz and Above—Part 1: Frequency Bands and Waveguide Dimensions*, Standard 1785.1-2012, 2012.
- [23] *IEEE Standard for Rectangular Metallic Waveguides and Their Interfaces for Frequencies of 110 GHz and Above—Part 2: Waveguide Interfaces*, Standard IEEE 1785.2-2016, 2016.
- [24] R. J. Cameron, C. M. Kudsia, and R. R. Mansour, *Microwave Filters for Communication Systems: Fundamentals Design and Applications*. New York, NY, USA: Wiley, 2018.
- [25] Fusion 360. *Autodesk*. Accessed: Jun. 25, 2023. [Online]. Available: <https://www.autodesk.co.uk/products/fusion-360/overview>
- [26] Chitubox. Accessed: Jun. 25, 2023. [Online]. Available: <https://www.chitubox.com/en>
- [27] Phrozen. Accessed: Jun. 25, 2023. [Online]. Available: <https://phrozen3d.com/products/phrozen-sonic-mini-8k-resin-3d-printer>
- [28] G. F. Engen and C. A. Hoer, "Thru-reflect-line: An improved technique for calibrating the dual six-port automatic network analyzer," *IEEE Trans. Microw. Theory Techn.*, vol. MTT-27, no. 12, pp. 987–993, Dec. 1979.
- [29] N. M. Ridler, R. G. Clarke, C. Li, and M. J. Salter, "Strategies for traceable submillimeter-wave vector network analyzer," *IEEE Trans. THz Sci. Technol.*, vol. 9, no. 4, pp. 392–398, Jul. 2019.
- [30] D. M. Pozar, *Microwave Engineering*, 3rd ed. New York, NY, USA: Wiley, 2005.
- [31] F. L. Warner, "Attenuation measurement," in *Microwave Measurements*, 2nd ed., A. E. Bailey, Ed. London, U.K.: IEE, 1989, pp. 132–134.
- [32] E. Hammerstad and O. Jensen, "Accurate models for microstrip computer-aided design," in *IEEE MTT-S Int. Microw. Symp. Dig.*, May 1980, pp. 407–409.
- [33] S. Lucyszyn, "RFIC and MMIC measurement techniques," in *Microwave Measurements*, 3rd ed., R. J. Collier and A. D. Skinner, Eds. London, U.K.: IET, Oct. 2007, pp. 217–262.
- [34] S. Papanonis and S. Lucyszyn, "Lossy spherical cavity resonators for stress-testing arbitrary 3D eigenmode solvers," *Prog. Electromagn. Res.*, vol. 151, pp. 151–167, 2015.
- [35] *Elegoo, Mars 4*. Accessed: Jun. 25, 2023. [Online]. Available: <https://www.elegoo.com/en-gb/products/elegoo-mars-4-msla-resin-3d-printer-with-9k-mono-lcd>



LIYAN ZHU received the B.Eng. degree in electronic science and technology from the Huazhong University of Science and Technology (HUST), Wuhan, China, in 2018, and the M.Sc. degree in telecommunications from University College London (UCL), London, U.K., in 2019. He is currently pursuing the Ph.D. degree with the Department of Electrical and Electronic Engineering, Imperial College London, London. His current research interests include the design, fabrication, and sensitivity analysis of microwave components using additive manufacturing techniques.



SANG-HEE SHIN (Member, IEEE) was born in Seoul, South Korea, in 1992. He received the M.Eng. degree in aeronautical engineering and the Ph.D. degree in electrical and electronic engineering from Imperial College London, London, U.K., in 2018 and 2022, respectively. He is currently a Higher Research Scientist with the Department of Electromagnetic and Electrochemical Technologies, National Physical Laboratory, U.K. His current research interests include designing and manufacturing RF and quasi-optical devices for microwave and millimeter-wave applications using additive manufacturing techniques.



ROSHAN PAYAPULLI received the M.Eng. and Ph.D. degrees in electrical and electronic engineering from Imperial College London, London, U.K., in 2018 and 2023, respectively. His current research interests include designing and manufacturing lightweight and low-cost waveguide components and systems for microwave and millimeter-wave applications using additive manufacturing techniques.



IAN W. ROSSUCK received the M.Eng. degree in electrical and electronic engineering from Imperial College London, London, U.K., in 2019, where he is currently pursuing the Ph.D. degree with the Department of Electrical and Electronic Engineering. He has two and half years of experience in the telecommunications industry as a radio frequency engineer, working on distributed antenna systems. His current research interests include the design and fabrication of (sub)millimeter-wave electronic devices using metalized polymer-based additive manufacturing and the biological effects of microwave radiation.



NORBERT KLEIN received the Diploma and Ph.D. degrees in physics from the University of Wuppertal, Wuppertal, Germany, in 1985 and 1989, respectively, and the Habilitation degree in physics from the Technical University of Aachen, Aachen, Germany, in 1998.

He was the Director of the Centre of Terahertz Science and Engineering, Imperial College London, London, U.K. Before 2009, he was the Division Leader of electromagnetic sensors with the Julich Research Center, Julich, Germany, and a Lecturer with the Technical University of Aachen and the Technical University of Dortmund, Germany. He is currently a Full Professor and the Chair of electromagnetic materials with Imperial College London. He is the (co)author of more than 172 peer-reviewed scientific articles and book articles with an H-index of 27 and is a key inventor on more than ten European and U.S. patents related to microwave devices for sensor and communication applications. In 2007, he founded a spin-off company which has successfully commercialized a microwave sensor system for airport security. His current research interests include microwave and terahertz sensors for biomedical and security applications and low-dimensional nanomaterials for high-frequency applications.



NICK M. RIDLER (Fellow, IEEE) received the B.Sc. degree from King's College London, University of London, London, U.K., in 1981. He is currently the Head of Science with the Electromagnetic and Electrochemical Technologies Department, National Physical Laboratory (NPL), U.K. He is also an Honorary Professor with the University of Glasgow and the University of Liverpool, U.K., and a Visiting Professor with the University of Kent, the University of Leeds, and

the University of Strathclyde, UK. He is also a Non-Executive Director of LA Techniques Ltd. He has more than 35 years of experience working in industrial, government, and academic research establishments. His current research interest includes precision high-frequency electromagnetic measurement (from 1 kHz to 1 THz). He is an NPL Fellow and a fellow of the Institution of Engineering and Technology (IET) and the Institute of Physics (IOP). He was the General Chair of the 2021 European Microwave Week.



STEPAN LUCYSZYN (Fellow, IEEE) received the Ph.D. degree in electronic engineering from King's College London, University of London, London, U.K., in 1992, and the D.Sc. degree (Higher Doctorate) in millimetre-wave and terahertz electronics from Imperial College London, London, in 2010.

He was the Director of the Centre of Terahertz Science and Engineering, Imperial College London, where he is currently a Professor of millimetre-wave systems. He co-founded Imperial College London spin-out company Drayson Wireless Ltd., in 2014. He has coauthored more than 200 articles and 12 book chapters in applied physics and electronic engineering. He was a fellow of the Institution of Electrical Engineers, U.K., and the Institute of Physics, U.K., in 2005. In 2008, he was a fellow of the Electromagnetics Academy, USA. He was appointed as an IEEE Distinguished Microwave Lecturer, from 2010 to 2013. In 2011, he chaired the 41st European Microwave Conference.

• • •